Photoluminescence of combinatorically sputtered Al_2O_3–Y_2O_3 thin films with a Cr^{3+} and Nd^{3+} co-doping concentration gradient

Derksen, Max; Bosco, Giacomo; Muller, Timo; van der Kolk, Erik

DOI
10.1016/j.jlumin.2024.120503

Publication date
2024

Document Version
Final published version

Published in
Journal of Luminescence

Journal of Luminescence 269 (2024) 120503

Contents lists available at ScienceDirect

Journal of Luminescence

journal homepage: www.elsevier.com/locate/jlumin

Full Length Article

Photoluminescence of combinatorically sputtered Al_2O_3–Y_2O_3 thin films with a Cr^{3+} and Nd^{3+} co-doping concentration gradient

Max Derksen [a,*], Giacomo Bosco [b], Timo Muller [a], Erik van der Kolk [a]

[a] Delft University of Technology, The Netherlands
[b] Fotoniq, The Netherlands

ARTICLE INFO

Keywords:
Reactive magnetron sputtering
Thin films
Al2O3–Y2O3
YAG, YAP, YAM
Chromium
Neodymium
Energy transfer
Luminescent solar concentrator

ABSTRACT

The characterization of a wide range of luminescent thin films can be a long and tedious endeavor. With reactive combinatorial sputtering of multiple metal targets, it possible to fabricate thin films with a gradient in composition simply by not rotating the substrate. In this work, combinatorically sputtered thin films of Cr^{3+} and Nd^{3+} doped in the Al_2O_3–Y_2O_3 system (YAlO) are studied for thin film based luminescent solar concentrators (TFLSCs) application. Contrary to mm's thick plate type LSC's, TFLSCs of just several 100 nm thick require much higher Cr^{3+} concentration to achieve 40% absorption which can enable several 10's of W/m^2 LSC power efficiencies. Our transmission measurements on a Cr_2O_3 film with a thickness gradient result in an absorption cross section at 460 nm of $1.3 \pm 0.7 \times 10^{-19}$ cm^2 showing that the TFLSC absorption requirement can be fulfilled provided that the Cr^{3+} concentration is in the order of 10^{22} ions/cm^3. The Y:Al ratio of the YAlO host in our films ranged between 0.5 and 3.5, thereby including the monoclinic ($Y_4Al_2O_9$), perovskite ($YAlO_3$) and garnet ($Y_3Al_5O_{12}$) stoichiometry's on a single film. Position dependent XRD, EDX, excitation, emission and lifetime measurements of Cr^{3+} and Nd^{3+} show that the unique gradient film sputtering method is able to characterize thin films as a function of host composition and doping concentration. Energy transfer between Cr^{3+} and Nd^{3+} in co-doped YAlO films is concluded from Cr^{3+} excitation bands observed while monitoring Nd^{3+} emission and from the matching of the rise-time of Nd^{3+} 1340 nm emission ($^4F_{3/2}$ -> $^4I_{11/2}$) and the decay time of Cr^{3+} 840 nm emission ($^4T_2$ -> $^4A_2$). Nd^{3+} lifetime systematically decreases from 0.24 to 0.05 ms with increasing Cr^{3+} concentration in $Y_3Al_{5-x}Cr_xO_{12}$:Nd ($0.05 < x < 2$). The constraints of heavily doped Cr^{3+} thin films for enabling adequate absorption and energy transfer to Nd^{3+} in TFLSC applications are the subjects of the discussion.

1. Introduction

Conventional luminescent solar concentrators (LSC's) are in the form of a single glass or polymer plate of several millimetres thick in which the luminescent species are introduced directly [1,2]. The plate acts as a sunlight absorbing waveguide in which generated luminescence light is guided to mounted solar cells at the edge. Thin film based luminescent solar concentrators (TFLSC's) fabricated via (reactive) magnetron sputtering are an attractive alternative design due to the compatibility with current glass industry large-scale coating capabilities. In general to achieve an LSC power conversion efficiency of 5–10% (i.e. several 10's of W/m2) with Si-solar cells there are three main criteria that must be met [3]:

i. Broadband UV to VIS absorption of around 40% at all wavelengths
ii. Minimum reabsorption losses due to overlap of absorption and emission.
iii. Near-unity photoluminescent quantum yield (PLQY) of the emission that is efficiently convertible to power by silicon solar cells.

Nd^{3+} satisfies the last two criteria, but not the first. The narrow, weak, forbidden 4f-4f transitions of the rare-earths do not provide adequate absorption. To accommodate for this, a strong and broad absorbing sensitizer can be used such as Cr^{3+}. The combination of Cr^{3+} and Nd^{3+} in glass has been considered for LSC applications in the conventional bulk plate configuration in the 1980s [4,5].

The Cr^{3+} concentration in these works was <1 mol.%, which would

* Corresponding author.
E-mail address: m.derksen-2@tudelft.nl (M. Derksen).

https://doi.org/10.1016/j.jlumin.2024.120503
Received 27 October 2023; Received in revised form 17 January 2024; Accepted 9 February 2024
Available online 15 February 2024

be too low in a thin film of several hundred nanometers considering condition (i). The absorption of a material can be calculated using equation (1), known as the Lambert-Beer law:

$$A = 1 - e^{-\alpha d} \quad (1)$$

Where α is the absorption coefficient (cm^{-1}) and d the film thickness (cm). It can be shown using the Lambert-Beer law, that the absorption coefficient of the thin film must be roughly 5000 cm^{-1} in order to achieve 40% internal absorption (excluding reflection or scattering losses) in a thin film with an industrial compatible thickness of 1 μm. α is simply the product of the concentration C of absorbing ions (cm^{-3}) and the absorption cross section σ (cm^2). Using Cr doped inside Al_2O_3, commonly known as ruby, as an example, we can find the necessary Cr^{3+} content to absorb approximately 40% within a 1 μm thin film. Because σ of Cr^{3+} at 430 nm in Al_2O_3 is 1.1×10^{-19} cm^2 [6], C must be around 4.5×10^{22} cm^{-3}, which is close to C of Al in Al_2O_3 (4.7×10^{22} cm^{-3}). This indicates that nearly all Al atoms must be replaced with Cr. This simple calculation shows that in order for TFLSC's to be efficient they must work with high concentrations of relatively strong absorbing species. Part of this work demonstrates a simple method to find the absorption cross section of Cr^{3+} using a single Cr_2O_3 thin film with varying thickness together with the Lambert-Beer law.

Although Al_2O_3 can accommodate a high concentration Cr^{3+} at the Al^{3+} sites, there is no available site for the much larger Nd^{3+} ion. Yttrium aluminate (Y_2O_3–Al_2O_3) provides a suitable site for both Cr^{3+} and Nd^{3+} and has been studied for numerous applications such as solid-state lasers, solar pumped lasers, luminescent thermometers and more [7–9]. Yttrium aluminate exists in three phases: monoclinic ($Y_4Al_2O_9$ or YAM), perovskite ($YAlO_3$ or YAP) and garnet ($Y_3Al_5O_{12}$ or YAG). The energy transfer between Cr^{3+} and Nd^{3+} has extensively been studied for YAG and YAP crystals with reported energy transfer efficiencies of 48 and 67% respectively [10–12]. The probability of energy transfer from Cr^{3+} was reported to be higher than that of non-radiative transitions of Cr^{3+}, indicating that the fluorescent quantum efficiency of Cr^{3+} is not a limiting factor in the maximum energy transfer efficiency [4,13]. Studies of Cr^{3+} luminescence as function of concentration in single doped Al_2O_3 has shown that Cr^{3+} emission quenches at concentrations <1 at.% due to the formation of Cr pairs that act as energy sinks [14,15]. Single Cr^{3+} ions can efficiently transfer energy amongst one another until it arrives at a Cr pair of which the decay rate is much faster, resulting in a quick dissipation of the energy. However it has been shown that incorporating another dopant such as Nd^{3+} allows to delay the Cr^{3+} concentration quenching effect [16]. Taken all together it is worth revisiting the Cr^{3+} and Nd^{3+} pair, in order to study their behavior in thin films with high concentration of Cr^{3+} which can provide adequate absorption and perhaps facilitate energy transfer to Nd^{3+}.

Studying luminescent properties of Y_2O_3, YAM, YAP, YAG and Al_2O_3 thin films doped with a range of Cr and Nd concentrations is a daunting task. However, using a unique approach that involves sputtering composition and doping concentration gradient thin films allows to analyze the behavior of the luminescence as a function of composition in a rapid fashion with a limited number of thin films. Our strategy is to use the gradient method to identify the optimum composition and subsequently when it is worthwhile to sputter homogeneous films with the same composition with other specialized sputtering systems. In this work we demonstrate the usefulness and validity of this gradient deposition technique as we explore the Al_2O_3–Y_2O_3 system doped with Cr^{3+} and Nd^{3+}. Rather than to investigate various properties of each phase of the Al_2O_3–Y_2O_3 system in detail, this work concerns itself with trends on single gradient films to underscore the power of the gradient method. We report on which phases of the Al_2O_3–Y_2O_3 system are most likely to form in thin films. The energy transfer between Cr^{3+} and Nd^{3+} as a function of host and Cr^{3+} concentration is qualitatively studied. We consider extreme cases where we replace 100% of Al with Cr in Cr_2O_3 and $YCrO_3$ thin films. Position dependent transmission, emission and lifetime measurements are provided and related to local composition. Finally a discussion is made on this gradient film method and the limitations of highly doped Cr^{3+} thin films to accommodate the necessary absorption and to facilitate energy transfer to Nd^{3+} for LSC applications.

2. Experimental details

2.1. Fabrication of thin films

A total of 9 samples were deposited on a non-rotating 44 × 44 × 1 mm^3 quartz substrate (except for one sample, CR08, which was deposited on a 50 × 50 × 1 mm^3 quartz substrate) using an AJA ATC Orion 5 magnetron sputtering system. Sputtering was done in a mixed atmosphere of oxygen and argon from four 2″ diameter and 1/4" thick targets: Y (99.9%), Al (99.999%), Cr (99.95%) and Nd (99.9%) (Demaco). Two pulsed direct current (DC) and two radio-frequency (RF) power supplies were used. Prior to deposition the sputter chamber is evacuated to a base pressure in the order of 0.1 mPa. The working pressure during sputtering is 0.4 Pa with a total gas flow of 15.0 sccm. The oxygen gas flow was chosen to be at the 'first critical point' identified through a typical hysteresis experiment [17]. The power on each target along with the O_2 flow was varied slightly between samples to acquire the desired compositions. Sputtering parameters used per sample can be seen in Table 1. The deposition time for CR01 to CR07 is 1500s and 2000s for CR08 and CR09, this deposition time was chosen to ensure a thickness below 1 μm. The working distance between target and substrate is 10 cm. The four targets are at right angles from one another, where each target is aligned so that the highest deposition rate is approximately at the edge of the substrate, in a sputter up configuration. In order to achieve doping concentrations between 1 and 10% of Cr a mask with holes is installed above the targets to reduce deposition rates by roughly 75 or 90%. For Nd, the magnetic strength of the magnetron is reduced to achieve doping concentration between 0.5 and 4%. For CR09 (Cr_2O_3), it has been shown that a substrate temperature of at least 500 °C is required to promote crystallinity which results in clear Cr^{3+} absorption [18]. The substrate is heated at 600 °C during deposition for all films and is not rotated in order to obtain a compositional gradient. A schematic can be seen in Fig. 1. The gradient Al_2O_3–Y_2O_3 films doped with Nd and Cr are given the name YAlO:Cr (x%) where x is the desired doping percentage of Cr in the center of the film, whereas the Nd concentration gradient was such that values never exceed 1 at.% anywhere in the film. After deposition, each sample was post annealed using a tube furnace at 1100 °C in an air atmosphere for 3 h. Annealing at these temperatures proved to be crucial in obtaining Cr^{3+} luminescence in the thin films.

Table 1
Sample specific sputter parameters used for the fabrication of the 9 thin films reported in this work. Common parameters are mentioned in the text. Sample names indicate their estimated doping Cr concentration at each film's center. All samples are estimated to have 1% Nd doping in the center except for CR02 and CR03 which have no Nd. *Mask placed on target to reduce deposition rate of Cr by roughly *70% or **90%. $^{\Delta}$No Nd in film. $^{+}$substrate of 50 × 50 × 1 mm^3 used instead of 44 × 44 × 1 mm^3.

ID	Layout	Composition	O2 (sccm)	Y/Al/Cr/Nd (W)
CR01	1	YAlO	1.9	120/120/0/25
CR02	1	YAlO:Cr (1%) $^{\Delta}$	1.6	110/130/90**/0
CR03	1	YAlO:Cr (10%) $^{\Delta}$	2	100/150/75*/0
CR04	1	YAlO:Cr (1%)	1.65	110/130/90**/25
CR05	1	YAlO:Cr (10%)	1.85	110/130/90*/25
CR06	1	YAlO:Cr (20%)	2.1	100/150/65/28
CR07	1	YAlO:Cr (40%)	3.3	100/150/110/40
CR08^{+}	2	YCrO3	2.2	135/0/110/20
CR09	2	Cr2O3	3	0/0/200/30

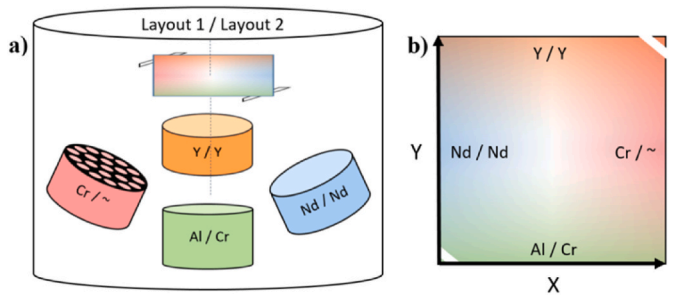

Fig. 1. a) schematic drawing of the sputter coater with the orientation of each source with respect to film orientation. Two layouts were used to acquire the desired concentration gradients. A mask was used on Cr for films with a low Cr concentration. b) The orientation of the films for each measurement with colour gradients to indicate the expected concentration gradient for each element.

2.2. Characterization of thin films

Energy-dispersive X-ray spectroscopy (EDS/EDX) measurements were done for 60 s using the JEAOL IT-100 EDX/SEM electron microscope at ×1000 magnification with an acceleration voltage of 12 kV, probe current of 60% and in a low vacuum pressure of 35 Pa.

X-ray diffraction (XRD) measurements were performed with a fixed slit width of 0.5 cm for half an hour using the PANalytical X'pert Pro MPD diffractometer. The equipment consists of a Cu Kα (1.54056 Å) anode which is operating at 45 kV and 40 mA.

Photoluminescence emission, excitation and lifetime measurements used a focused optical parametric oscillator OPO EKSPLA/NT230 laser as excitation source with a pulse duration of 3–6 ns FWHM. Excitation wavelength is tunable between 193 and 2600 nm. A beam splitter is used to re-direct part of the laser to the sample, whilst the transmitted part is read out by Thorlabs thermal power meter to correct for the power of the laser in excitation measurements modes. The laser is focused with a converging lens, however the sample is placed slightly further from the focal point to avoid laser damage due to high power density, the laser spot size is approximately 2 mm in diameter. Appropriate cut-off filters were used to remove the laser observed in second order from emission measurements. The collection of the emission is optimized via two lenses where the sample is located in the focal point of the first lens, the first lens is located two focal lengths away of the second lens and finally an optical fiber is one focal length away of the second lens. The optical fiber is connected to either an Ocean Optics QE Pro (400–1100 nm) or the NIRQuest 512 (900–1600 nm) spectrometer for emission/excitation measurements. For lifetime measurements the optical fiber is connected to either a Hamamatsu R7600U-20 (300–920 nm sensitivity) or Hamamatsu H10330A-75 (950–1700 sensitivity) photomultiplier tube both operating at 800V which is subsequently read out by a CAEN DT5724 digitizer after a trigger pulse from the EKSPLA laser.

All measurements, except for XRD measurements, were performed by placing the sample on two translation stages at right angles with precise position read-out. EDS measurements are made on a 5 × 5 grid whilst photoluminescence measurements are done on a 21 × 21 grid. This allowed us to directly link the local compositions of the film to the local photo-luminescent properties. Further details on this method can be found in previous work [19].

3. Results & discussion

3.1. Thin film composition

The concentration (at. %) of Nd in film CR01 is presented in Fig. 2a. Per film, a total of 25 points in a 5 × 5 grid were measured using EDS. Two dimensional linear interpolation and extrapolation were used to retrieve the concentration across the entire film. The corresponding color bar is shared with Fig. 2b at the top. A clear gradient is observed

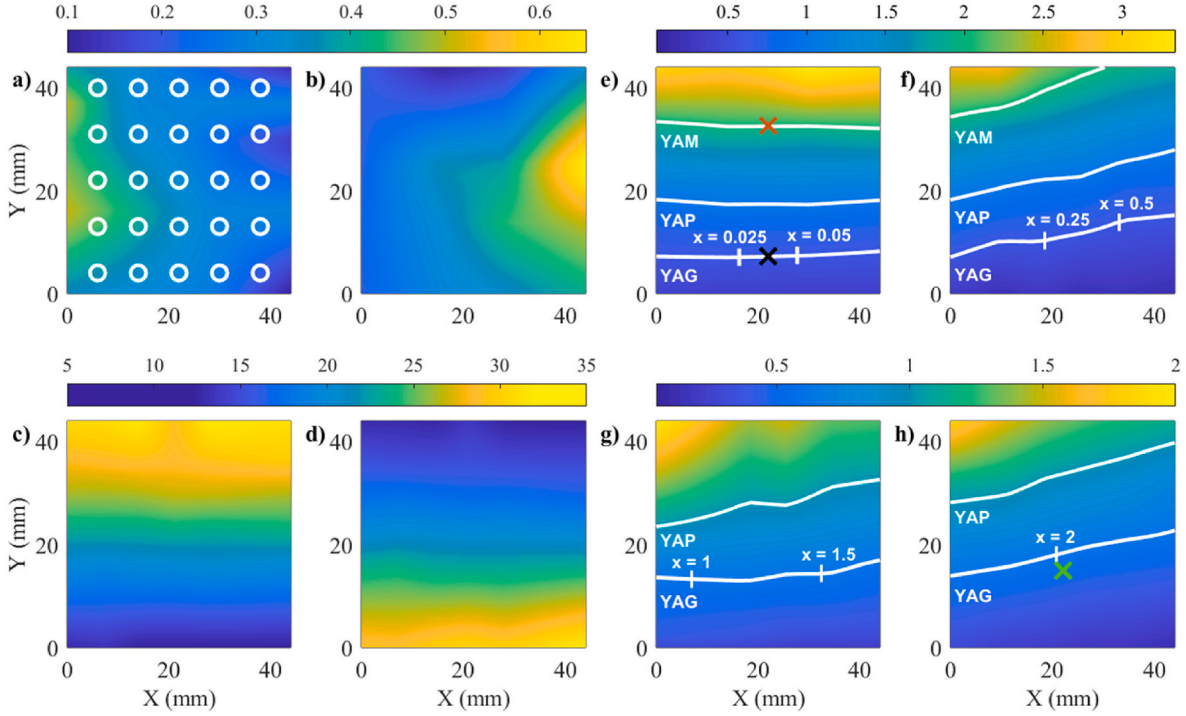

Fig. 2. a) Heat map of the concentration (at.%) of Nd in CR01, the color bar is shared with b. b) Concentration of Cr (at.%) of CR02. c) and d) concentration of Y and Al (at.%) in CR01 respectively. e), f), g) and h) ratio between Y and Al + Cr of CR04, CR05, CR06 and CR07 respectively. YAM, YAP and YAG stoichiometry's, where Y:(Al + Cr) are 2, 1 and 0.6, are respectively indicated by the white contour lines. Vertical markers on the YAG contour line indicate number of Al atoms replaced by Cr out of 5 (i.e. $Y_3Al_{5-x}Cr_xO_{12}$). Colored 'X' markers - in black and red in c) and green in f) – indicate where XRD measurements were performed. XRD diffractograms are shown in Fig. 3.

with increasing Nd content from right to left; however the gradient is not particularly smooth. This is due to the relatively poor accuracy of EDS for low concentrations. Yet the accuracy is more than enough to verify the expected Nd composition trends increasing from right to left. It can be concluded that the Nd concentration is always below 1 at.% throughout the film and increases approximately linearly from right to left between 0.1 and 0.8 at. %. This linear relationship in concentration with a stationary substrate has also been shown in previous work [20]. The concentration range of Nd was chosen below 1% to prevent any cross relaxation between Nd^{3+} atoms which typically occurs at concentrations above 1% [21]. Similarly, in film CR02, the Cr concentration is between 0.1 and 0.7 at. % as shown in Fig. 2b. Fig. 2c and d shows the Y and Al concentration of CR01 respectively and share a different color bar. For the YAlO:Cr, Nd samples (CR01 – CR07), the Nd, Y and Al concentration distribution are fairly constant. Fig. 2a–d demonstrate nicely that the alignment of the sputter coater is in such a way that each element is edge-focused to the corresponding side of the substrate, i.e. Nd on the left, Cr on the right, Y at the top and Al at the bottom. The Cr concentration was then systematically increased in the co-doped films series, from CR04 to CR07. Within a single film the Cr concentration increases from left to right. In Fig. 2e–h, the Y:(Al + Cr) ratio is shown for CR04 – CR07. It is possible to get the Y:(Al + Cr) stoichiometry ratio, y, of the three well-known crystal structure phases with y = 2, 1 and 0.6, for YAM, YAP and YAG respectively, on a single film indicated by the white contour lines in Fig. 2e–h. Note that the white contour lines are purely based on measured stoichiometry and are not on the crystal structure patterns. XRD results are presented in the following section. The Y:(Al + Cr) ratio for CR05, CR06 and CR07 are shown in Fig. 2f, g and h respectively. Markers are placed on the contour lines of the YAG ($Y_3Al_{5-x}Cr_xO_{12}$) stoichiometry to indicate certain doping concentrations of Cr^{3+} where x = 0.025, 0.05, 0.25, 0.5, 1, 1.5 and 2 which correspond to doping percentages of 0.5%, 1%, 5%, 10%, 20%, 30% and 40% respectively. From a compositional point of view, these four films (CR04, CR05, CR06 and CR07) can be used to study the Al_2O_3–Y_2O_3 system with low atomic concentrations of Nd (<1%) and large range of doping concentrations of Cr (0.025–40%) within only 4 films. Similarly to the Y:(Al + Cr) ratio, for CR08 the Y:Cr ratio varied linearly from bottom to top in the range of 0.5–3 but these results are not shown. CR09 simply contained Cr_2O_3 and thus only varied in thickness. Both CR08 and CR09 showed similar Nd content ranging between 0.1 and 0.8 at.% from right to left.

3.2. Phase identification of thin films

Fig. 3 shows XRD measurements done on specific spots on the CR04, CR07, CR08 and CR09 samples. CR08 and CR09 show as expected characteristic peaks corresponding to the intended $YCrO_3$ and Cr_2O_3 phases. CR08 required annealing to promote crystallinity as the as deposited sample was amorphous. CR09 showed crystallinity as deposited and improved on XRD peak intensity after a post anneal treatment.

As shown by the EDS results, we get the stoichiometry of the three main phases of the Al_2O_3–Y_2O_3 system on a single film. However, the correct stoichiometry does not necessarily translate to the appropriate corresponding phase. One part $Y_3Al_5O_{12}$ and one part Y_2O_3 yields a Y:Al ratio of 1 without the YAP phase present. The YAP phase was not identified through XRD measurements anywhere in the samples. The $YCrO_3$ phase, unlike YAlO3, was clearly measured, as shown in Fig. 3. The reason for this can be that Y_2O_3–Al_2O_3 is more likely to form the YAG or YAM phases, whereas Y_2O_3–Cr_2O_3 only has the $YCrO_3$ phase and their respective individual phases (Y_2O_3 and Cr_2O_3). Growing YAP on silica glass has been successful in other work but it was found that using a perovskite substrate promoted a higher chance of success [22]. Prior to annealing, the CR01-CR07 films were amorphous. Upon annealing, the peaks in the XRD diffractogram were present primarily belonging to the YAM and YAG phases. Of all the phases, YAG was most prominent throughout the CR01-CR07 films. Two measurements were done on

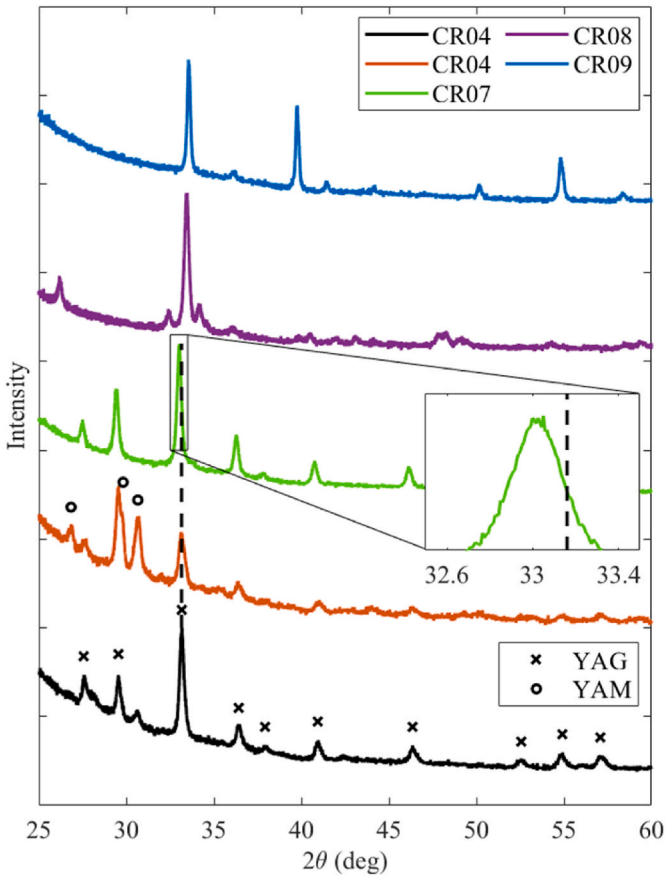

Fig. 3. XRD measurements of samples CR04, CR07, CR08 and CR09. The black, red, and green plots are measured at their corresponding-colored markers in Fig. 2e and h. An inset provides a closer look at the peak shift occurring due to Cr doping. Markers of the YAG and YAM peaks are taken from ICDD reference 04-008-3458 and 04-011-4887 respectively. In blue and purple samples CR08 and CR09 are measured and a close match to the CR2O3 and YCrO3 phase is found when compared to references 01-078-5443 and 01-081-8632 respectively.

CR04 at the bottom and top of the sample (indicated by a black and red marker in Fig. 2e. Towards the bottom of the film where the stoichiometry resembles that of YAG, the phase is almost exclusively YAG with some YAM. Contrary to the top of the film we see YAG peaks lose intensity whilst YAM peaks increase in intensity, which is as expected when looking at the Y:(Al + Cr) ratio.

Towards the bottom of the CR04 film (indicated by a black 'x' in Fig. 2c the amount of Cr is roughly 0.05, whereas in CR07, at the green 'x' marker in Fig. 2h, it is roughly 2. The peak around 33° is shifted by 0.12° to the left. Replacing Al with Cr leads to a larger lattice due to the Cr ion being bigger than Al. This results in a shift in the XRD peaks to the left, which is shown in the inset in Fig. 3. This observed shift indicates that Cr successfully takes the place of Al in the YAG phase.

3.3. Chromium absorption

In Fig. 4a–a series of transmission spectra are plotted from the top to the bottom of the Cr_2O_3:Nd sample (CR09). Nd^{3+} absorption is not observed due to the weak, parity-forbidden, 4f-4f transitions of trivalent lanthanides. Two clear absorption bands from Cr^{3+} can be seen centred around 460 and 600 nm which are attributed to the spin-allowed ^4A to $^4T_{1g}$ and $^4T_{2g}$ transitions which have been reported for Cr in various compounds [23]. At lower energies there are the spin forbidden transitions ^4A to $^2T_1$ and ^2E, also known as the ruby lines or R-lines, which are not observed but have been reported elsewhere [23]. The absorption

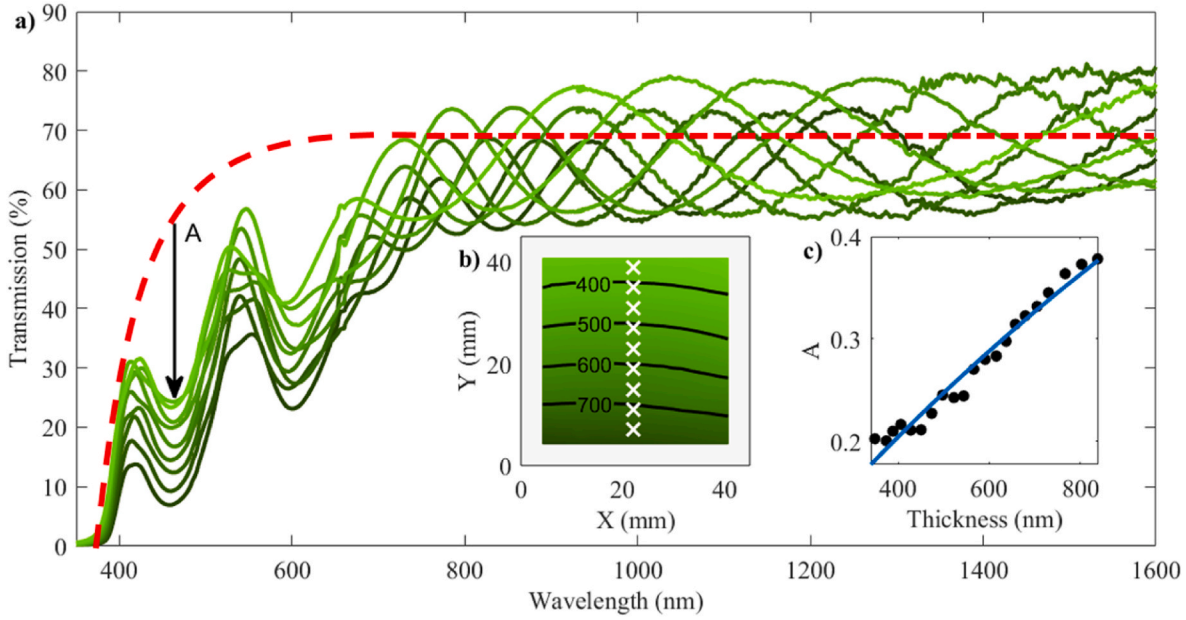

Fig. 4. a) transmission measurements of CR09 taken along the arrow in b). The dotted line represents an estimation of the average scattering and reflection losses. The green arrow represents absorption due to Cr^{3+}. b) a heat map of the film thickness. c) thickness plotted against absorption for 21 points from top to bottom in the center of the film. These points are fitted with the Lambert Beer law in blue.

below 400 nm is attributed to the optical band-gap which is a result of a charge transfer transition between the 2p oxygen valence band atoms and the Cr^{3+} 3d conduction band [23,24]. This charge-transfer absorption prevents the higher energy spin allowed transition ^4A to $^4T_1$ to be observed. In Fig. 1b the thin film interference fringes in the region of 800–1600 nm are fitted at 21 × 21 points using a combination of the software package OPTIFIT [24,25] and in-house built software that automates the fitting procedure for each point as described in Refs. [19,27]. Optical constants, n and *k*, and the thickness are retrieved across the entire film. The thickness ranges in between 350 (at the far side from the Cr target) and 840 nm (at the near side from the Cr target). A thickness map is plotted in Fig. 4b. The refractive index was found to be around 2.4 ± 0.1 at 586 nm over the whole film. The refractive index is a close match to other fabricated Cr_2O_3 thin-films [18,28]. An estimation of the transmission of a bulk-like Cr_2O_3 film, generated by the n and k dispersion relation, given by Refs. [26,27], is shown by the red dotted line. This line indicates the (Mie) scattering and (Fresnel) surface reflection losses. By taking the scattering and reflection loss into account it is possible to estimate the absorption caused by the Cr^{3+} transition bands, indicated by the black arrow. Here we look at the absorption at 460 nm. The thickness plotted against this estimated absorption is plotted in Fig. 2c. At thicknesses below 700 nm there appear oscillations in a similar fashion to the transmission data which is due to thin film interference. At thicknesses above 700 nm, this behaviour ceases due to the increased absorption, leaving insufficient light to affect the transmission data with thin film interference. This data has been fitted shown in blue using the Lambert-Beer law (equation (1)) to find an absorption coefficient of 5.4×10^3 cm^{-1} at 460 nm. Using the molar mass of Cr to be 152 g/mol and the bulk density of 5.22 g/cm^3 the concentration of Cr ions is 4.1×10^{22} cm^{-3}. Assuming this concentration is constant over the film we find an absorption cross section of $1.3 \pm 0.7 \times 10^{-19}$ cm^2. This uncertainty comes from the estimation in the scattering losses. Note that the density of the thin film has not been measured and can deviate (often lower) from the bulk density. Despite these uncertainties, this result corresponds well with what has been reported for Cr^{3+} absorption cross sections found in ruby, which is 1.1×10^{-19} cm^2 [6,29].

In Fig. 5, the transmission spectra as function of Cr content are shown. Measurements for the YAlO films (CR04 – CR07) where taken at the white vertical markers shown in Fig. 2e–h. The transmission of

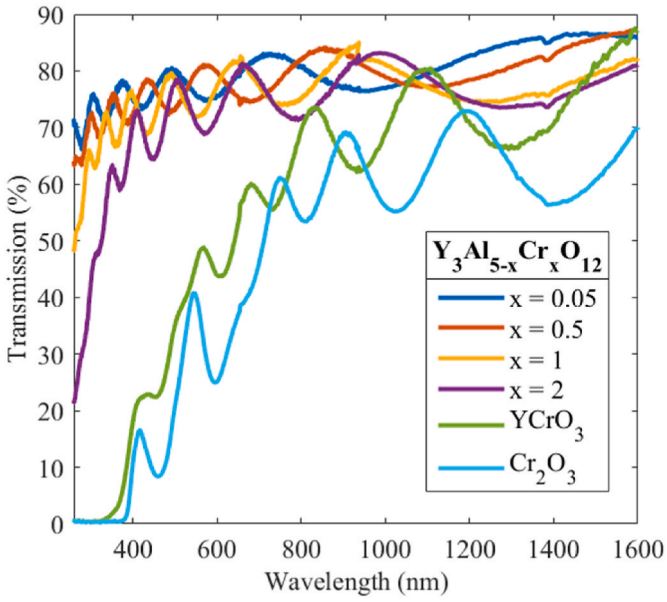

Fig. 5. Transmission spectra taken from samples CR04-CR09. The specific positions on the films of the measurements for CR04-CR07 are shown via the vertical markers in Fig. 2e–h. At wavelengths 655 and 933 there are discontinuity due artefacts caused by an intense sharp peak from the deuterium light source and combining the spectra from two separate spectrometer respectively.

$YCrO_3$ was measured where the Y:Cr ratio was 1:1. The charge transfer absorption of Cr below 400 nm becomes stronger with higher content, ultimately leading to match the optical bandgap in Cr_2O_3. The lower energy bands of Cr^{3+} at 430 and 600 nm are clearly visible in Cr_2O_3 and $YCrO_3$, however at lower concentrations it is difficult to observe due to the thin film interference effects. Optical properties are again fitted using the OPTIFIT method and are shown in Table 2. Increasing Cr content also leads to a higher refractive index. These results are shown in Table 2. The theoretical absorption is calculated using the Lambert-Beer law with the absorption cross section found earlier along with thickness

Table 2
Refractive index (n) and thickness (d) retrieved through fitting of the thin film interference fringes. Concentrations of Cr^{3+} are used to estimate film absorption taking the Cr^{3+} absorption cross-section of Fig. 4c.

$Y_3Al_{5-x}Cr_xO_{12}$	n	c (cm^{-3})	d (nm)	A (460 nm)
x = 0.05	1.76	2.3×10^{20}	412	0.002
x = 0.5	1.78	2.3×10^{21}	480	0.02
x = 1	1.85	4.6×10^{21}	519	0.045
x = 2	1.91	9.2×10^{21}	521	0.09
$YCrO_3$	2.16	1.8×10^{22}	782	0.25
Cr_2O_3	2.17	4.1×10^{22}	780	0.47

found through fitting and the concentrations calculated through the theoretical molecular weight and density of YAG (593 g/mol and 4.6 g/cm^3), $YCrO_3$ (189 g/mol, 5.7 g/cm^3) and Cr_2O_3 (152 g/mol, 5.2 g/cm^3).

In this section we have shown through XRD, EDS and optical measurements that these gradient thin films are of consistent quality and can be used to investigate the required concentration of Cr^{3+} in order to obtain adequate absorption for thin film based LSC applications. Results show that 100% Cr^{3+}concentration is required in order to achieve 40% absorption at 460 nm for films with thickness below 1 μm. In the next section we investigate the luminescence behaviour of low concentrations of Nd^{3+} inside the Al_2O_3–Y_2O_3 system, with no Cr^{3+}present.

3.4. Single doped gradient neodymium film (YAlO:Nd^{3+})

In Fig. 6 an excitation- and emission spectrum, taken at the centre of the film CR01 is presented. Sample CR01 has a similar composition to CR04 that was presented in Fig. 2c, with the exception that no Cr^{3+} is present. The Y:Al ratio varied between 3.5 and 0.3 from top to bottom (Fig. 2c), whereas the Nd^{3+} concentration ranged between 0.1 and 0.6 at. % from right to left (Fig. 2a). Typical Nd^{3+} 4f-4f excitation and emission transitions are present. The main emission lines are grouped around 885, 1060 and 1340 nm and correspond to transitions from the $^4F_{3/2}$ manifold to the $^4I_{9/2}$, $^4I_{11/2}$, $^4I_{13/2}$ levels respectively. In Fig. 6b a heat map is presented of the intensity of the 885 nm emission. Unfortunately, the intensity observed is not only dependent on the intrinsic luminescence properties of the material but also on the out-coupling efficiency controlled by film morphology and surface roughness which is difficult to correct for. The shape of the emission is however unaffected by the these out-coupling effects and can therefore be compared between different locations at the film. In Fig. 6c three spectra are shown on the top and bottom of the film indicated by the x in Fig. 6b. At the top of the film, where the YAM phase is dominant, we see that the emission peak of the $^4F_{3/2}$ -> $^4I_{11/2}$ transition is located at 1058 nm, which is consistent with previous reported literature [29]. Towards the bottom of the film, spectra more related to YAG are observed with a well-known peak at 1064 nm used for laser applications. Both spectra have a broad emission underneath their peaks indicating that inhomogeneous broadening is taking place - which is likely due to amorphous phases being present in the sample. It should be noted that the emission spectrum in Fig. 6a was obtained by two spectrometers. A spectrum from an Ocean Optics QE Pro (400–1100 nm) and a NirQuest (900–1600 nm) were connected at 900 nm. The spectra have been corrected for their corresponding detector efficiencies. The Ocean Optics QE Pro spectrometer has a higher wavelength resolution, allowing for more detailed photoluminescence structures, and was therefore used for the measurements in Fig. 6c.

Similarly to the shape of the emission, the lifetime of the emission is independent of the out-coupling efficiency. The radiative lifetime measurements at four locations on the film – indicated by Fig. 7b - are shown in Fig. 7a. The lifetime is not mono-exponential and therefore a mean lifetime is calculated instead using the formula:

$$\frac{\int_0^\infty t\Phi_t(t)dt}{\int_0^\infty \Phi_t(t)dt} \tag{2}$$

where t is time after excitation (at t = 0) and $\varphi_t(t)$ is the time-resolved luminescence intensity. We see that the radiative lifetime ranges from 0.1 to 0.5 ms from bottom to top. These results are consistent with reported literature where the lifetime of Nd^{3+} in YAG (bottom of the film) is around 0.24 ms and that of YAM is 0.6 ms [20,30]. These results demonstrate that this gradient method can be used to study trends as a function of varying host composition. The Nd^{3+} lifetime from right to

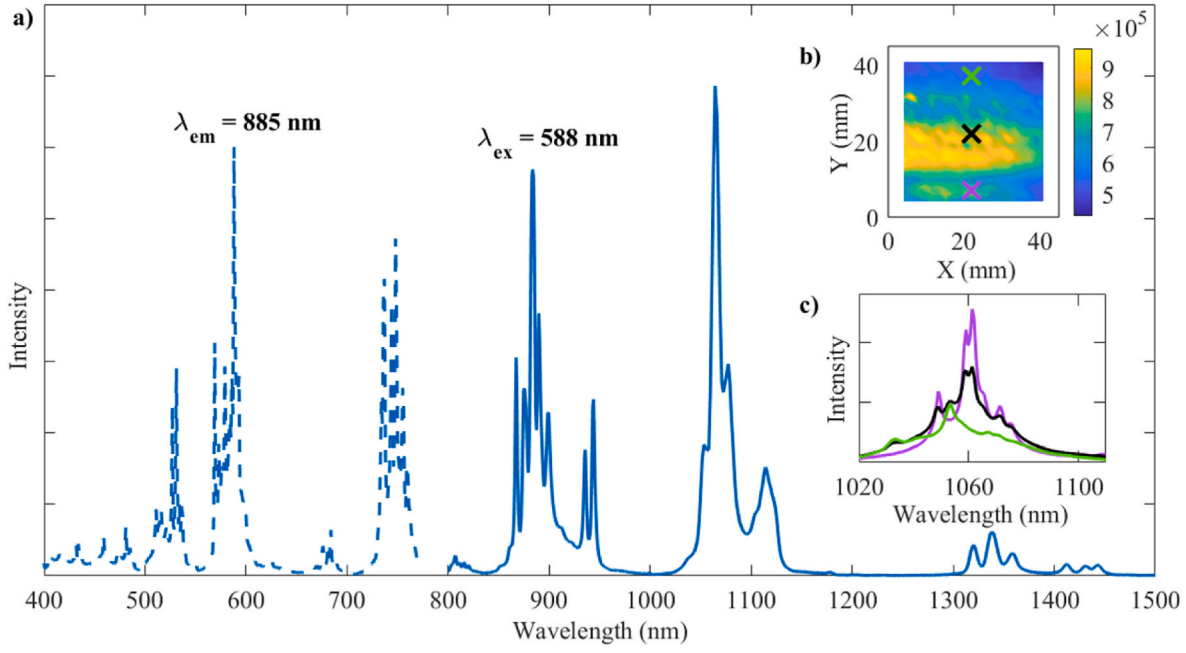

Fig. 6. a) excitation-emission spectra of CR01 when excited in the center of the film. b) heat map of the λ_{em} = 1064 nm intensity of nm Nd^{3+}. c) Emission spectra of Nd^{3+} with λ_{ex} = 588 nm at two positions on the film indicated by the corresponding colored markers in b.

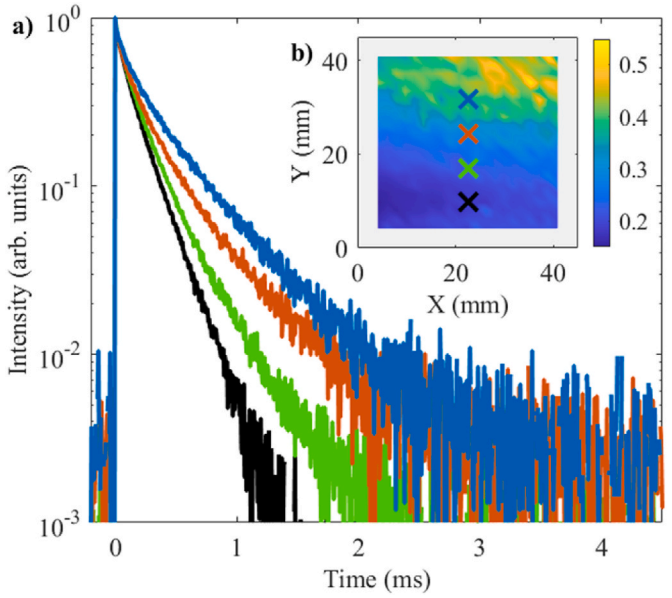

Fig. 7. a) Series of lifetime measurements of $\lambda_{em} = 1064$ nm of Nd^{3+} with $\lambda_{ex} =$ 588 nm, measurements are taken of CR01 on locations indicated via corresponding colored markers shown in b. b) Heat map showing the mean decay time in ms across the entire CR01 sample.

left, where the Nd concentration increases from 0.1 to 0.6 at.%, remains constant, indicating that there is no concentration quenching occurring within the film. Later, when we look at the co-doped materials, we can exclude cross-relaxation between Nd^{3+} ions to be a cause of non-radiative transitions.

3.5. Chromium doped gradient films ($YAlO:Cr^{3+}$)

For the $YAlO:Cr^{3+}$ films, CR02 and CR03, the Cr content increases from left to right from 0.1 to 0.7% (Figs. 2b) and 0.6–3% respectively. The Y:Al ratio increased from bottom to top in the range of 0.4–3.5 in both films (similar to Fig. 2c). The excitation and emission spectra taken at the centre of the CR02 film is shown in Fig. 8a. In the excitation spectra we see two bands centred around 430 and 600 nm which are associated with the $^4A_2$ to $^4T_1$ and $^4T_2$ transitions observed earlier in the transmission data of Cr_2O_3 film. The emission closely resembles that of $YAG:Cr^{3+}$ which is elsewhere reported [31]. The main R line from the ^2E to $^4A_2$ electronic transition is at 688 nm which has vibronic sideband with peaks at 709 and 725 nm. The R-line of $YAP:Cr^{3+}$ is situated around the vibronic sideband of $YAG:Cr^{3+}$ at 725 nm. The vibronic sidebands of the R-line in $YAP:Cr^{3+}$ at longer wavelengths have a peak around 750 nm [31], which is not observed anywhere in the sample. Combining this observation with the lack of YAP-related XRD peaks shows clearly that no $YAP:Cr^{3+}$ is present anywhere in the sample. A key difference in the emission compared to earlier results is the longer wavelength sideband. Previous studies show that the vibronic sideband of the R line extends to no more than 800 nm [31]. However, we observe emission up until roughly 975 nm. This broad emission at longer wavelength is likely to be caused by Cr^{3+} ions situated at a site with a low ligand field strength for which the $^4T_{2g}$ level lies below the ^2E level, resulting in broad and redshifted emission. Similar emission is reported for glasses doped with Cr^{3+} [5], indicating that an amorphous phase is also present in our films.

Fig. 8b shows a heat map of the emission around 709 nm when excited at 435 nm. Again, due to the difficulty of correcting for out-coupling efficiencies, no definite statement can be made about where, in the composition space, the sample has the highest emission efficiency. However, it can be noted that towards the top of the sample, where the YAM phase is dominant, there is close to no luminescence observed. In Fig. 8c–a photograph of the sample is shown where one can see regions on the film that appear more diffuse or transparent. A horizontal stripe just below the centre of the film appears more transparent (i.e less scattering and lower out-coupling of the emission) which corresponds to the lower emission area in the heat map in Fig. 8b.

In Fig. 9a, the decay curves of the 707 nm emission, excited with 430 nm, on 4 different locations on the CR02 film are shown. The radiative lifetime was calculated at 11 × 17 points across the film and shown in Fig. 9b. The top part of the sample is not presented as there was no luminescence observed as shown in Fig. 8b. The radiative lifetime decreases from the bottom left (Cr poor, Al rich region) to the top right (Cr rich, Al poor region) which is consistent with the expectations of concentration quenching effects.

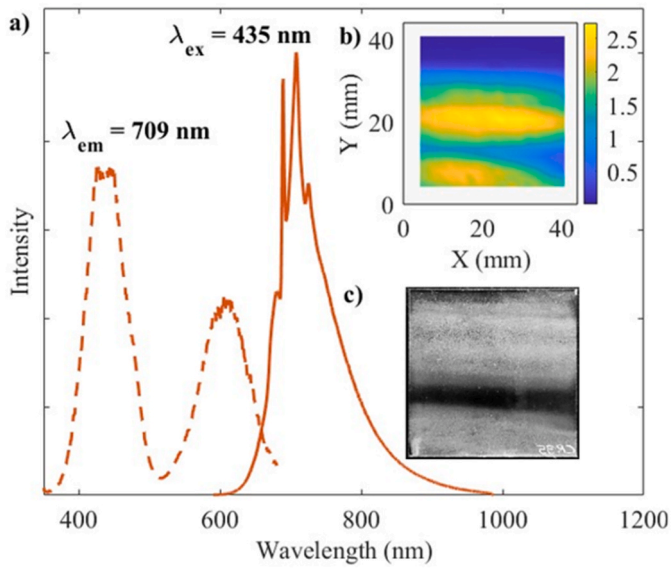

Fig. 8. a) Excitation-emission spectra taken at the center of CR03. b) heat map of the $\lambda_{em} = 707$ nm intensity. c) black and white photo of film CR02 showing the position dependent scattering nature of the film.

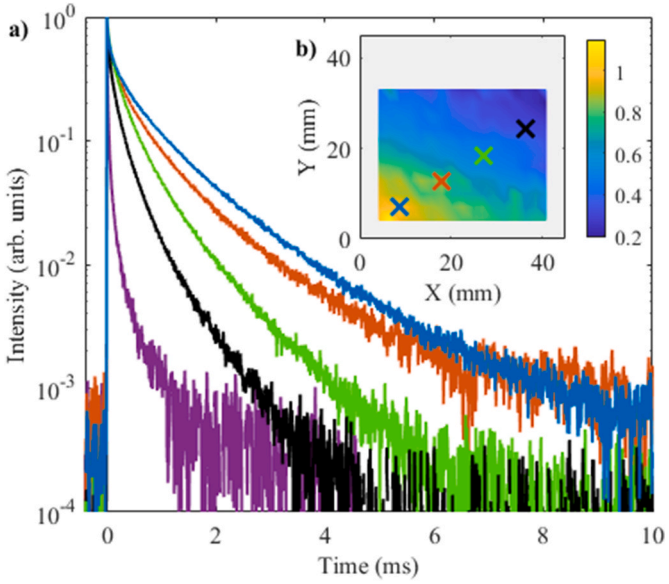

Fig. 9. a) Cr^{3+} lifetime measurements for $\lambda_{em} = 707$ nm with $\lambda_{ex} = 430$ nm of CR02 taken at the position indicated by the marker with their corresponding color in b). One measurement of the Cr^{3+} lifetime in CR03 is shown in purple, where the Cr content is 1.5 at.%. b) heat map of the radiative lifetime across the film.

An additional lifetime measurement of CR03 is shown in purple in Fig. 9a at a location for which the estimated Cr content is 1.5 at.% with a Y:Al ratio of 0.6 (YAG). The mean lifetime according to equation (1) is found to be 0.08 ms. The bottom left corner of CR02 has a lifetime around 1 ms (shown in blue in Fig. 9a), this position also has the YAG ratio, but the Cr content is estimated to be 0.1 at.%. This decrease in lifetime due to concentration quenching has been extensively studied in the past and is contributed to Cr–Cr pairs and Cr clusters acting as quenching centers [14,15]. These exchange coupled Cr–Cr pairs start to form at concentrations >0.5 at%. Previous studies show a radiative lifetime of the R-line emission of Cr^{3+} to be 1.7 ms at 0.5 at.% [16,32], indicating significant radiative losses in the bottom left corner of CR02. This can be caused by mixed phases and defects present in the material.

So far we have looked at the Al_2O_3–Y_2O_3 system doped separately with Nd^{3+} and Cr^{3+}. On single films we explained luminescent behaviour as function of host and concentration of both Nd^{3+} and Cr^{3+}. To further test this gradient film method, we now co-dope the films with Cr^{3+} and Nd^{3+} and investigate the energy transfer from Cr^{3+} to Nd^{3+} as a function of Cr^{3+} concentration.

3.6. Double doped thin films ($Y_3Al_{5-x}Cr_xO_{12}$)

In Fig. 10, the excitation and emission spectra taken at x = 0.05 and x = 0.5 ($Y_3Al_{5-x}Cr_xO_{12}$) of films CR04 and CR05 are presented. By monitoring the Nd^{3+} 1060 nm emission, we can clearly see the two broad bands of Cr^{3+}, providing evidence that energy transfer is taking place. For x = 0.05 there remain Nd^{3+} 4f-4f lines (around 530 and 588 nm) observed on top of the broad Cr^{3+} bands. This indicates that the Nd^{3+} emission when excited via Cr^{3+} is comparable in intensity to the direct excitation of Nd^{3+}. Generally, the emission is equal to the product of absorption, the energy transfer efficiency (if applicable) and the quantum yield. The observed comparable emission intensity when exciting through Cr^{3+} or directly into Nd^{3+} shows that the efficiency of the energy transfer must be low as the absorption of the spin-allowed Cr^{3+} transition is much stronger than that of the parity forbidden 4f-4f transitions of Nd^{3+}. This is with the assumption that the quantum yield of Nd^{3+} remains unchanged with the introduction of Cr^{3+}. However, at x = 0.5 (CR05), Cr^{3+} absorption dominates due to the higher concentration of Cr^{3+} and the 4f-4f lines are hardly detectable which is

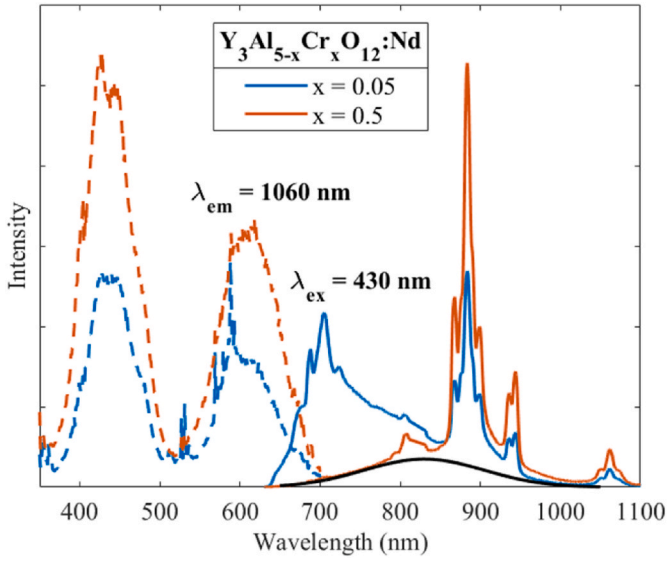

Fig. 10. Excitation (λ_{em} = 1060 nm) and emission spectra (λ_{ex} = 430 nm) of CR04 and CR05 taken at positions indicated by the vertical markers, shown in Fig. 2c and d. Their stoichiometries ($Y_3Al_{5-x}Cr_xO_{12}$:Nd) are x = 0.05 and x = 0.5. The solid black line represents emission from Cr^{3+} ions situated at sites with low ligand field fitted with a Gaussian function (using an eV scale).

observed in Fig. 10a. The Cr content increases by a factor 10 from CR04 and CR05, which increases the Cr^{3+} absorption at 460 nm by a factor of 10 as shown in Table 2. The intensity of the excitation of Nd^{3+} at 460 nm increases roughly by a factor 2, indicating that the energy transfer efficiency from Cr^{3+} to Nd^{3+} has decreased by a factor 5 with the increased Cr^{3+} content. This can be a result from the formation of Cr pairs and clusters acting as quenching centers discussed in section 3.5. Furthermore, we can see from the solid blue plot (x = 0.05) in Fig. 10a, that with λ_{ex} = 430 nm the emission consists of YAG:Cr^{3+}, YAG:Nd^{3+} and a broad band emission with a peak centred around 840 nm as shown by the solid black fitted curve to guide the eye. The broad emission has been attributed to the $^4T_2$ -> $^4A_2$ transition for Cr^{3+} situated at sites with low ligand field strength. When increasing the Cr from x = 0.05 to x = 0.5 in YAG:Cr^{3+}, the YAG:Cr^{3+} emission is fully quenched. Despite that the quenched YAG:Cr^{3+} emission, there is still energy transfer taking place, as evidenced by the characteristic Cr^{3+} bands in the excitation spectra. The broad band emission remains present in the emission spectra at the higher Cr concentration. To investigate the origin of the energy transfer between Cr^{3+} and Nd^{3+}, radiative lifetime measurements are performed and presented in the following section.

In Fig. 11a we see the time resolved intensity of the Cr^{3+} R-line (λ_{em} = 707 nm) for the singly doped YAG:Cr^{3+} (CR02) and doubly doped YAG:Cr^{3+}, Nd^{3+} thin film (CR04) shown in red and blue respectively. Measurements were done at the location for both films where the YAG stoichiometry was x = 0.05 which is shown with a marker labelled x = 0.05 in Fig. 2c. The mean lifetime of R-line Cr^{3+} emission for double doped YAG:Cr^{3+}, Nd^{3+} was found to be 0.2 ms. This is four times shorter than the mean lifetime of the singly doped Cr^{3+} film CR02 which has a mean lifetime of around 0.8 ms. The decrease of the radiative lifetime is mainly caused by the introduction of a fast component which dominates until about t > 0.2 ms. However, the tail (>1 ms) of the Cr^{3+} emission can be well fitted with a single exponential with a lifetime of 0.8 ms (R-square = 0.9907), similar to the mean lifetime of the single-doped Cr^{3+} films. This suggests that energy transfer is taking place between the R-line and Nd^{3+} 4f states in the first 0.2 ms. When comparing the lifetime of the Nd^{3+} emission in the single doped YAG:Nd^{3+} (CR01) with the double doped YAG:Nd^{3+}, Cr^{3+} (CR04), shown in Fig. 11b in red and blue respectively, it can be seen that there is indeed a rise time for the double doped YAG:Nd^{3+}, Cr^{3+}. However, this rise time appears much shorter than the fast component of the Cr^{3+} emission. Generally, if energy transfer occurs between a donor (Cr^{3+}) and acceptor (Nd^{3+}) where the lifetime of the donor (0.8 ms) is longer than that of the acceptor (0.24 ms) one would expect the lifetime of the acceptor to be the same as the lifetime of the donor. For the Cr^{3+} Nd^{3+} system, it has been shown in previous studies that the Nd^{3+} lifetime has been reported to lengthen, from 0.24 to 0.4 ms due to energy transfer from the R-line of Cr in YAG [16]. In our case the mean lifetime of the Nd^{3+} 1340 nm emission when excited through Cr^{3+} is found to only slightly increases to 0.26 ms. Taken together, the reduction in the Cr^{3+} R-line mean lifetime in our sample does not appear to be caused by the energy transfer to Nd^{3+}. The origin of this fast component has not been studied but can be the result of increased quenching centers caused by a poor incorporation of Nd^{3+} in the film.

In Fig. 11c the lifetime of the broad Cr^{3+} emission ($^4T_2$ -> $^4A_2$) around 840 nm is compared to the lifetime of the 1340 nm emission of Nd^{3+} when excited at 435 nm. This broad emission of Cr^{3+} has a mean lifetime of 54 μs, which is much shorter than the R-line. This is due to the spin-allowed nature of the transition. We see that the rise time of Nd^{3+} matches closely to the decay of this broad emission. Therefore, energy transfer appears to mainly take place between the low crystal field sites and Nd^{3+} rather than between Cr^{3+} ions at regular lattice sites in YAG. The observed energy transfer between the broad emission of Cr^{3+} and Nd^{3+}, rather than between the R-line of Cr^{3+} and Nd^{3+}, makes sense when considering the better spectral overlap between the emission and absorption of Cr^{3+} and Nd^{3+} respectively and has been noted before [4].

Lastly, the mean radiative lifetime of Nd^{3+} is measured as a function

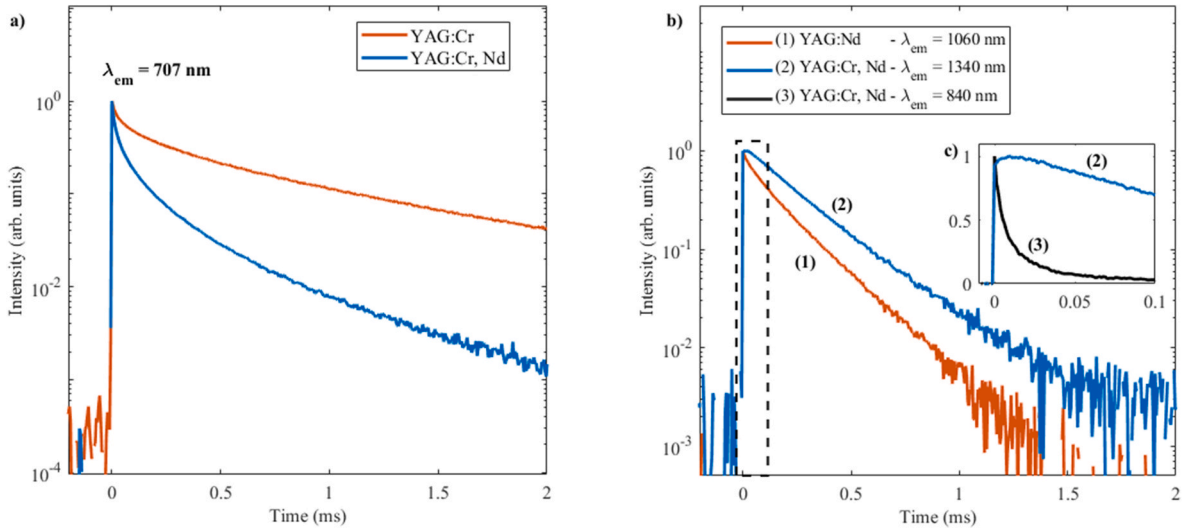

Fig. 11. a) Radiative lifetime of the Cr^{3+} R-line^{+} (λ_{em} = 707 nm) in single doped YAG:Cr^{3+} and double doped YAG:Cr^{3+}, Nd^{3+} with λ_{ex} = 620 nm. b) Radiative lifetime of the Nd^{3+} $^4F_{3/2}$ manifold (λ_{em} = 1060 and 1340 nm) in single doped YAG:Nd^{3+} and double doped YAG:Cr^{3+}, Nd^{3+} with λ_{ex} = 588 nm and λ_{ex} = 620 nm respectively. c) A shorter timeframe that includes the radiative lifetime of the broad Cr^{3+} emission around 840 nm in YAG:Cr^{3+}, Nd^{3+} with λ_{ex} = 620 nm. All measurements were taken at locations with a YAG stoichiometry of x = 0.05 as shown in Fig. 2c.

of Cr^{3+} concentration in the YAG part of the films. In Fig. 12 we measure the lifetime of Nd^{3+} as a function of x ($Y_3Al_{5-x}Cr_xO_{12}$) when exclusively exciting Cr^{3+} at 435 nm. At low Cr concentration (x < 0.2) the mean lifetime of Nd^{3+} is between 0.24 and 0.28 ms. The slightly longer mean lifetime of Nd^{3+} in YAG:Cr^{3+}, Nd^{3+} over single doped YAG:Nd^{3+} is likely due to the added rise time of Nd^{3+} without suffering of subsequent quenching. However, increasing the Cr^{3+} concentration further leads to a systematic decrease in Nd^{3+} lifetime. The Nd concentration was kept low (<0.1 at%) to eliminate cross relaxation between Nd^{3+} ions to be a cause in drop of lifetime. The reduction in Nd^{3+} lifetime can be caused by the incorporation of Cr^{4+} inside the tetrahedral Al site in the YAG phase. Cr^{4+} has broad absorption around 1000 nm which can cause energy transfer from Nd^{3+} to Cr^{4+} [22]. If Cr^{3+} situated in low ligand field strength sites are nearby Nd^{3+} then energy transfer can also occur between the $^4F_{3/2}$ and the $^4T_2$ of Nd^{3+} and Cr^{3+} respectively. Other culprit candidates are the host material which can have defects and mixed phases. An extensive study to investigate this quenching routes has not been done.

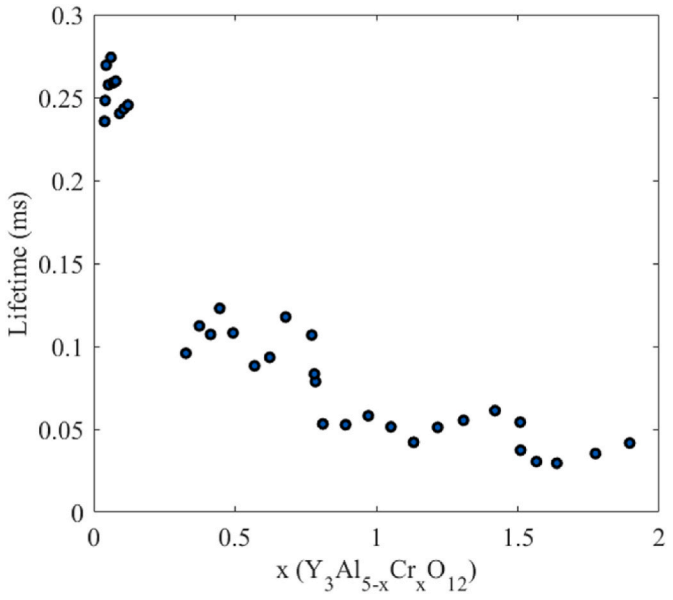

Fig. 12). Radiative lifetime of nm Nd^{3+} emission (λ_{em} = 1340 nm) as function of Cr content.

The aim of this work was to investigate further the interplay of strong Cr^{3+} absorption and subsequent energy transfer and emission of Nd^{3+}. In Fig. 12 the Nd^{3+} lifetime drops to 0.05 ms at Cr^{3+} concentration of 10 at.% (x = 2) in YAG. To increase the Cr^{3+} further the $YCrO_3$ (20 at.% Cr^{3+}) and Cr_2O_3 (40 at.% Cr^{3+}) host were briefly studied. In the Cr_2O_3 and $YCrO_3$ films doped with Nd^{3+} there was no emission of Nd^{3+}, regardless of exciting exclusively in Cr^{3+} or Nd^{3+}. It appears that fully concentrated Cr^{3+} systems like $YCrO_3$ and Cr_2O_3, do provide the desired absorption but are unable to facilitate energy transfer to Nd^{3+}.

4. Conclusion

In this work we have provided, using the gradient sputtering approach, evidence that it is possible to acquire >40% Cr^{3+} absorption within a <1 μm thin film with a fully concentrated Cr^{3+} system i.e. Cr_2O_3.

The Al_2O_3–Y_2O_3 system was chosen to study the luminescent behavior of Cr^{3+} and Nd^{3+} both independently doped and co-doped. On a single film, via gradient sputtering, the Y:Al ratio varied between 0.5 and 3.5 which encompasses the stoichiometry of the YAG, YAP and YAM phases. XRD measurements showed YAG and YAM phases were present. No YAP phase was detected. Position dependent emission and lifetime measurements of Al_2O_3–Y_2O_3 gradient films doped with Nd^{3+} corroborated previously observed behavior of Nd^{3+} emission and lifetime across the films going from the YAM to the YAG dominant part of the film indicating the good quality of our films. The main emission peak ($^4F_{3/2}$ -> $^4I_{11/2}$) shifts from 1058 nm (YAM:Nd^{3+}) to 1064 nm (YAG:Nd^{3+}). The lifetime of the $^4F_{3/2}$ level decreases from 0.6 to 0.24 ms typically for YAM:Nd^{3+} and YAG:Nd^{3+} respectively on a single film. These results demonstrate the unique value of this gradient method to study luminescent thin films.

Al_2O_3–Y_2O_3 doped with Cr^{3+} showed characteristic YAG:Cr^{3+} emission with an R-line (^2E -> $^4A_2$) emission at 707 nm. A broad emission in the near infrared ($^4T_2$ -> $^4A_2$) was also observed in the films. The mean lifetime of the R-line Cr^{3+} emission in YAG was found to be 0.8 ms and shortened to 0.2 ms towards the Cr^{3+} rich part of the film.

More data was provided on the Al_2O_3–Y_2O_3 system doped with both Nd^{3+} and Cr^{3+} in order to investigate the energy transfer between Cr^{3+} and Nd^{3+} in the various identified phases. Excitation spectra have shown

that Nd^{3+} can be excited through Cr^{3+}. Increasing Cr^{3+} from 1% doping to 10% doping in YAG part of the film improved absorption of Cr^{3+} but reduced energy transfer efficiency to Nd^{3+}, potentially due to Cr pairs and clusters. The observed rise-time of the Nd^{3+} emission intensity was found to match the decay of the broad-band emission of Cr^{3+}, rather than that of the R-line. The energy transfer therefor appears to take place between the Cr^{3+} ions situated at sites with low ligand field strength and Nd^{3+}. Finally, fully concentrated Cr_2O_3 and $YCrO_3$, though promising due to their absorption, showed no energy transfer to Nd^{3+} and appear to be ill-suited for thin film based LSC applications. Energy transfer was studied between Cr^{3+} and Nd^{3+} as function of Cr^{3+} concentration. At high concentration (>0.5 at.%) of Cr^{3+}, in the YAG part of the thin-films, the Nd^{3+} lifetime systematically decreased from 0.25 to 0.05 ms, possibly due to transfer to Cr^{4+} or due to back-transfer to Cr^{3+} situated at low ligand field strength sites, which has been previously reported. The combination of reduced energy transfer to Nd^{3+} due to the Cr pairs/clusters and back-transfer from Nd^{3+} to $Cr^{3+/4+}$ limits their use in thin film based LSC's.

CRediT authorship contribution statement

Max Derksen: Data curation, Formal analysis, Investigation, Visualization, Writing – original draft. **Giacomo Bosco:** Conceptualization, Supervision, Validation, Writing – review & editing. **Timo Muller:** Methodology. **Erik van der Kolk:** Formal analysis, Funding acquisition, Supervision, Validation, Writing – review & editing.

Declaration of competing interest

The authors declare that they have no known competing financial interests or personal relationships that could have appeared to influence the work reported in this paper.

Data availability

Data will be made available on request.

Acknowledgments

This work was supported by the Netherlands Organization for Scientific Research (NWO/OCW), as part of the High-Tech Systems and Materials (HTSM) program with project number NWO:17105.

References

[1] W.H. Weber, J. Lambe, Luminescent greenhouse collector for solar radiation, Appl. Opt. 15 (1976) 2299–2300, https://doi.org/10.1364/ao.15.002299.
[2] J.S. Batchelder, A.H. Zewai, T. Cole, 'Luminescent Solar Concentrators 1: theory of operation and techniques for performance evaluation', Appl. Opt. 18 (1979) 3090–3110, https://doi.org/10.1364/ao.18.003090.
[3] B.C. Rowan, L.R. Wilson, B.S. Richards, Advanced material concepts for luminescent solar concentrators, IEEE J. Sel. Top. Quant. Electron. 14 (5) (2008) 1312–1322, https://doi.org/10.1109/jstqe.2008.920282.
[4] R. Reisfeld, Future technological applications of rare-earth-doped materials, Journal of the Less Common Metals 93 (2) (1983) 243–251, https://doi.org/10.1016/0022-5088(8390163-7.
[5] B. Jeżowska-Trzebiatowska, E. Łukowiak, W. Stręk, A. Buczkowski, S. Patela, J. Radojewski, J. Sarzyński, Neodymium-chromium doped phosphate glasses as luminescent solar concentrators, Sol. Energy Mater. 13 (4) (1986) 267–277, https://doi.org/10.1016/0165-1633(8690002-x.
[6] E.H. Penilla, C.L. Hardin, Y. Kodera, S.A. Basun, D.R. Evans, J.E. Garay, The role of scattering and absorption on the optical properties of birefringent polycrystalline ceramics: modeling and experiments on ruby ($Cr:Al_2O_3$), J. Appl. Phys. 119 (2) (2016) 023106, https://doi.org/10.1063/1.4939090.
[7] Z.J. Kiss, R.J. Pressley, Crystalline solid lasers, Proc. IEEE 54 (10) (1966) 1236–1248, https://doi.org/10.1109/proc.1966.5112.
[8] T. Saiki, K. Imasaki, S. Motokoshi, C. Yamanaka, H. Fujita, M. Nakatsuka, Y. Izawa, Disk-Type Nd/Cr:YAG ceramic lasers pumped by arc-metal-halide-lamp, Opt Commun. 268 (1) (2006) 155–159, https://doi.org/10.1016/j.optcom.2006.07.002.
[9] L. Marciniak, A. Bednarkiewicz, J. Drabik, K. Trejgis, W. Strek, Optimization of highly sensitive YAG:Cr^{3+},Nd^{3+} nanocrystal-based luminescent thermometer operating in an optical window of biological tissues, Phys. Chem. Chem. Phys. 19 (10) (2017) 7343–7351, https://doi.org/10.1039/c6cp07213e.
[10] J.A. Mareš, W. Nie, G. Boulon, Multisites and energy transfer in Cr^{3+}-Nd^{3+} codoped $Y_3Al_5O_{12}$ and $YAlO_3$ Laser Crystals, J. Phys. 51 (15) (1990) 1655–1669, https://doi.org/10.1051/jphys:0199000510150165500.
[11] S.R. Rotman, E. Luria, E. Herman, A. Shohan, J.A. Mares, G. Boulon, A. Brenier, L. Lou, Fast energy transfer from donor pairs to single acceptors in a Cr^{3+}, Nd^{3+}-doped $YAlO_3$ crystal, Opt. Mater. 13 (1) (1999) 63–65, https://doi.org/10.1016/s0925-3467(99)00012-9.
[12] M.J. Weber, Chromium—rare-earth energy transfer in $YAlO_3$, J. Appl. Phys. 44 (9) (1973) 4058–4064, https://doi.org/10.1063/1.1662895.
[13] J.A. Mareš, Z. Khás, W. Nie, G. Boulon, Nonradiative energy transfer between Cr^{3+} and Nd^{3+} multisites in $Y_3Al_5O_{12}$ laser crystals, J. Phys. 1 (6) (1991) 881–899, https://doi.org/10.1051/jp1:1991174.
[14] G.F. Imbusch, Energy transfer in ruby, Phys. Rev. 153 (2) (1967) 326–337, https://doi.org/10.1103/physrev.153.326.
[15] G.F. Imbusch, Energy transfer in heavily-doped ruby, J. Lumin. 53 (1–6) (1992) 465–467, https://doi.org/10.1016/0022-2313(92)90199-j.
[16] K. Fujioka, T. Saiki, S. Motokoshi, Y. Fujimoto, H. Fujita, M. Nakatsuka, Luminescence properties of highly Cr co-doped Nd:YAG powder produced by sol–gel method, J. Lumin. 130 (3) (2010) 455–459, https://doi.org/10.1016/j.jlumin.2009.10.012.
[17] K. Strijckmans, R. Schelfhout, D. Depla, Tutorial: hysteresis during the reactive magnetron sputtering process, J. Appl. Phys. 124 (24) (2018) 241101, https://doi.org/10.1063/1.5042084.
[18] P. Hones, M. Diserens, F. Lévy, Characterization of sputter-deposited chromium oxide thin films, Surf. Coating. Technol. 120–121 (1999) 277–283, https://doi.org/10.1016/s0257-8972(99)00384-9.
[19] E.P.J. Merkx, E. van der Kolk, Method for the detailed characterization of co-sputtered inorganic luminescent material libraries, ACS Comb. Sci. 20 (11) (2018) 595–601, https://doi.org/10.1021/acscombsci.8b00068.
[20] Y. Deng, J.D. Fowlkes, J.M. Fitz-Gerald, P.D. Rack, Combinatorial thin film synthesis of Gd-doped $Y_3Al_5O_{12}$ ultraviolet emitting materials, Appl. Phys. A 80 (4) (2005) 787–789, https://doi.org/10.1007/s00339-003-2385-0.
[21] L.D. Merkle, M. Dubinskii, K.L. Schepler, S.M. Hegde, Concentration quenching in fine-grained ceramic Nd:YAG, Opt Express 14 (9) (2006) 3893–3905, https://doi.org/10.1364/oe.14.003893.
[22] Y. Shimizu, K. Ueda, F. Massuyeau, S. Jobic, Preparation of thin films of perovskite-type $YAlO_3$:Gd^{3+} – Pr^{3+} UV phosphors, Thin Solid Films 571 (2014) 90–93, https://doi.org/10.1016/j.tsf.2014.09.075.
[23] R.S. Pavlov, V.B. Marzá, J.B. Carda, Electronic absorption spectroscopy and colour of chromium-doped solids, J. Mater. Chem. 12 (9) (2002) 2825–2832, https://doi.org/10.1039/b201802k.
[24] A.N.L. Jara, J.F. Carvalho, A.F. Júnior, L.J.Q. Maia, R.C. Santana, On the optical and magnetic studies of $YCrO_3$ Perovskites, Phys. B Condens. Matter 546 (2018) 67–72, https://doi.org/10.1016/j.physb.2018.07.026.
[25] R. Alvarez, A. Garcia-Valenzuela, C. Lopez-Santos, F.J. Ferrer, V. Rico, E. Guillen, M. Alcon-Camas, R. Escobar-Galindo, A.R. Gonzalez-Elipe, A. Palmero, 'High rate deposition of stoichiometric compounds by reactive magnetron sputtering at oblique angles', plasma process, Polym 13 (2016) 960–964, https://doi.org/10.1002/ppap.201600019.
[26] R. Swanepoel, Determination of the thickness and optical constants of amorphous silicon, J. Phys. E Sci. Instrum. 16 (12) (1983) 1214–1222, https://doi.org/10.1088/0022-3735/16/12/023.
[27] E.P.J. Merkx, S. van Overbeek, E. van der Kolk, Functionalizing window coatings with luminescence centers by combinatorial sputtering of scatter-free amorphous SiAlON:Eu^{2+} thin film composition libraries, J. Lumin. 208 (2019) 51–56, https://doi.org/10.1016/j.jlumin.2018.12.011.
[28] M.F. Al-Kuhaili, S.M.A. Durrani, Optical properties of chromium oxide thin films deposited by electron-beam evaporation, Opt. Mater. 29 (6) (2007) 709–713, https://doi.org/10.1016/j.optmat.2005.11.020.
[29] D.M. Dodd, D.L. Wood, R.L. Barns, Spectrophotometric determination of chromium concentration in ruby, J. Appl. Phys. 35 (4) (1964) 1183–1186, https://doi.org/10.1063/1.1713590.
[30] W. Ryba-Romanowski, R. Lisiecki, A. Rzepka, L. Lipińska, A. Pajączkowska, Luminescence and excitation energy transfer in rare earth-doped $Y_4Al_2O_9$ nanocrystals, Opt. Mater. 31 (8) (2009) 1155–1162, https://doi.org/10.1016/j.optmat.2008.12.006.
[31] K.M. Kinsman, J. McKittrick, E. Sluzky, K. Hesse, Phase development and luminescence in chromium-doped yttrium aluminum garnet (YAG:Cr) phosphors, J. Am. Ceram. Soc. 77 (1994) 2866–2872, https://doi.org/10.1111/j.1151-2916.1994.tb04516.x.
[32] Z.Y. Zhang, K.T.V. Grattan, Temperature dependence of YAG:Cr^{3+} fluorescence lifetime up to 550 K, J. Lumin. 62 (6) (1994) 263–269, https://doi.org/10.1016/0022-2313(94)90046-9.